Check for updates

Nitrogen-doped graphene–TiO$_x$N$_y$ nanocomposite electrode for highly efficient capacitive deionization†

Yuchen Wu,[ab] Gaopeng Jiang, [ID] [b] Qian Li,[b] Zisheng Zhang,[*a] and Zhongwei Chen [ID] [*b]

In this work, the first-ever reported nanocomposite electrode of nitrogen-doped graphene–titanium oxynitride (NG–TiO$_x$N$_y$) for capacitive deionization (CDI) was synthesized *via* hydrothermal reaction and a high-temperature nitridation process. The physiochemical characterizations revealed that the nitrogen was doped in the graphene structure mainly in the form of graphitic nitrogen and the TiO$_x$N$_y$ was successfully formed *via* TiO$_2$ nitridation process. The layered NG nanosheets facilitated the diffusion of ions in saline water and formed electrical double layer on the surface of the electrode material, while the presence of TiO$_x$N$_y$ enhanced the electrochemical performance by increasing surface area and generating surface vacancies *via* nitridation. The CDI cell employed NG–TiO$_x$N$_y$ electrode delivered a breakthrough salt adsorption capacity of 26.1 mg g^{-1} in 500 mg L^{-1} saline water, and retained over 90% of its initial salt removal efficacy after 12 regeneration cycles. Such high CDI performance exhibits the promising application of NG–TiO$_x$N$_y$ as a novel CDI electrode candidate.

1 Introduction

Obtaining fresh and clean water is one of the most urgent environmental problems in the 21st century.[1] An effective solution for increasing the fresh water supply is to develop sustainable desalination technology, which can treat brackish and saline water.[2] However, traditional water desalination techniques including distillation, reverse osmosis, and vacuum evaporation are approaching their limitations as they require high operating temperature, huge energy consumption, and large capital cost.[3] Alternatively, capacitive deionization (CDI) has become one of the most promising solutions for water desalination,[4] which works by separating and adsorbing ions on each electrode. It has the advantageous nature of high efficiency, low cost, low energy-consumption, ambient atmosphere operation, and environmental-benignity.[5] The electrode material in a CDI cell plays a pivotal role in determining the desalination performance.[6] Currently, most reported and commercialized CDI electrode materials are based on various kinds of novel porous carbon electrodes.[7–14]

Graphene, as a novel two-dimensional carbon nanomaterial, has been widely used as the electrode materials in batteries and

supercapacitors due to its high electrochemical performance and large surface area.[15–20] Its heteroatom-doped derivative, especially nitrogen-doped graphene (NG), has also been investigated as electrode materials to achieve even better electrochemical performance in batteries and supercapacitors as opposed to graphene due to nitrogen-doped active sites and enhanced electrical conductivity.[21,22] It is also worth to notice that it is reported that by nitrogen doping, the NG achieved significantly high adsorption capacity in CDI test.[23–28] On the other hand, titanium oxynitride (TiO$_x$N$_y$, where x and y stand for the unspecific atom ratios of oxygen and nitrogen to titanium, respectively) and/or titanium nitride (TiN) can be fabricated into nanomaterials and used as electrodes materials in batteries and supercapacitors with enhanced electrochemical performance and wettability.[29–31] Additionally, with various morphologies, various Ti species and excellent electrical performance, TiN and/or TiO$_x$N$_y$ can be used as additives to enhance the performance of graphene nanosheets by forming nanocomposites.[32,33] Moreover, our previous research disclosed that the porous TiN/TiO$_x$N$_y$ had shown excellent performance as the CDI electrode material.[34] However, there is no reported nanocomposites of NG and TiO$_x$N$_y$ that have been synthesized and used as CDI electrode materials. Therefore, it is highly promising to prepare this kind of hybrid material and investigate its potential performance in CDI devices for water desalination.

In this study, a first-ever reported nanocomposite electrode of nitrogen-doped graphene–titanium oxynitride (NG–TiO$_x$N$_y$) was synthesized *via* the hydrothermal reaction and high-temperature nitridation process and then tested for CDI. The physiochemical

^{a}Department of Chemical and Biological Engineering, University of Ottawa, 161 Louis Pasteur Private, Ottawa, Ontario K1N 6N5, Canada. E-mail: Jason.zhang@uottawa.ca
^{b}Department of Chemical Engineering, University of Waterloo, 200 University Ave W, Waterloo, Ontario N2L 3G1, Canada. E-mail: zhwchen@uwaterloo.ca

† Electronic supplementary information (ESI) available. See DOI: 10.1039/c9ra05380h

characterization results demonstrated the successful formation of nitrogen-doped-sites on the graphene nanosheets and the TiO_xN_y nanoparticles embedded on the graphene nanosheets. The multi-layered graphene structure and TiO_xN_y nanoparticles allowed the saline water stream to pass through and facilitates a fast ion diffusion process to form the electrical double layer (EDL) at the electrode interface of both the graphene layers and TiO_xN_y nanoparticles. As a result, the $NG–TiO_xN_y$ electrode delivered a significantly higher salt removal efficiency than the commercial AC, pure rGO and $rGO–TiO_2$ electrodes in single-pass CDI test (Fig. 1). Furthermore, the electrode reached a maximum salt adsorption capacity of 26.1 mg g^{-1} in 500 mg L^{-1} feed in saline water. The electrode material also exhibited great regeneration capacity and long-life cycling stability. The overall superior results demonstrated that the $NG–TiO_xN_y$ could be an ideal CDI electrode material candidate.

2   Experimental

2.1   Synthesis of TiO_2 nanoparticles

The synthesis procedure of the polystyrene (PS) nanosphere is adapted from the literature.[35] First, 2.5 g polyvinylpyrrolidone (PVP, M.W. 10 000) was charged in a three-neck flask that contains 200 mL boiled distilled deionized water (oxygen-free DDI). After PVP was fully dissolved, the flask was placed in an oil bath with N_2 gas purging under the surface of the solution to expel the oxygen in the system. As the temperature was elevated to 70 °C for 15 min, styrene monomer (24 mL) was gradually added into the flask for 20 min with vigorous stirring and refluxing. Then, the potassium persulfate (40 mL, 5 mg mL^{-1}) was dropwise added into the mixture, and the emulsion polymerization was continued under an air-free atmosphere at 70 °C for 24 h. The PS emulsion was centrifuged and washed with DDI water for several times. Then, after 3 days' freeze-drying, the PS nanospheres were obtained.

Titanium(IV) butoxide (TBOT, 97%, 10 mL), ethanol (>99%, 10 mL), and hydrochloric acid (37%, 2 mL) were mixed with a volume ratio of 5 : 5 : 1 and stirred for at least 30 min. Meanwhile, 2 grams of the PS nanosphere was sonicated and re-dispersed in 20 mL ethanol. The PS nanosphere ethanol

dispersion was then added into the TBOT solution and the mixture was sonicated until it turns light yellow after 30 min[36–38] After drying the sol–gel in ambient conditions overnight, the composite sample was loaded into a tube furnace and subjected to sequential heat treatments at 300 °C for 1 h and 540 °C for 30 min under argon atmosphere to form the TiO_2 nanoparticles.

2.2   Synthesis of $NG–TiO_xN_y$

In this study, the GO and TiO_2 were mixed in designed mass ratios (1 : 1, 2 : 1, and 3 : 1) in a beaker with 400 mL DDI water and thoroughly stirred for over 24 hours. Then, the mixed solution was sealed in an autoclave and hydrothermally treated for 12 h at 180 °C. The hydrotreated product was then centrifuged at 2500 rpm and separated from the solution. Subsequently, the product was washed by DDI water and centrifuged several times. The obtained product was then oven dried at 60 °C for 12 h, and then transferred to a vacuum oven and fully dried. Thus, in this step, GO was reduced to rGO[39] and the obtained composite is denoted as $rGO–TiO_2$ for comparison.

The dried composite was transferred to a ceramic boat and was subjected to heat treatment from room temperature to 800 °C with a ramp rate of 1 °C min^{-1} under argon flow. Then, the atmosphere was switched from argon to ammonia after the temperature reached 800 °C and was kept at 800 °C for 1 h to proceed the nitridation. Then, the sample was cooled down until room temperature in argon.

2.3   Physicochemical and electrochemical characterization

The crystal structure property of the electrode material was characterized by X-ray diffraction (XRD, RIETVELDXRG 3000) and the chemical composition was characterized by X-ray photoelectron spectroscopy (XPS, Thermo Scientific K-Alpha spectrometer) at University of Waterloo. Sample morphology was examined using scanning electron microscopy (SEM, ZEISS ULTRA PLUS), and transmission electron microscopy (TEM, Carl Zeiss Libra 200MC STEM).

The crystallite size was calculated according to the Scherrer equation, given in eqn (1):

$$\tau = \frac{K\lambda}{\beta \cos \theta} \tag{1}$$

where τ is the dimension of the crystallites; K is a dimensionless shape factor, approximately 0.89; λ is the wavelength of X-ray, which is 1.54 Å; β is the line broadening at half the maximum intensity, which is 0.185; and θ is the Bragg angle.

Cyclic voltammetry (CV) measurements were employed for evaluating the electrochemical performance of the CDI electrode and its adsorption/desorption capacity. The CV experiment was performed in a three-electrode system, which employed a carbon electrode as the counter electrode and a saturated calomel electrode (SCE) as the reference electrode in the NaCl electrolyte solution. Reversible Hydrogen Electrode (RHE) were used to calibrate the SCE electrode in a pH = 7 NaCl solution, as shown in Fig. S1 in the ESI.† The actual potential was calibrated by add 0.5 V to the original value, where the potential range from −1 V to 0 V is corresponded to the actual
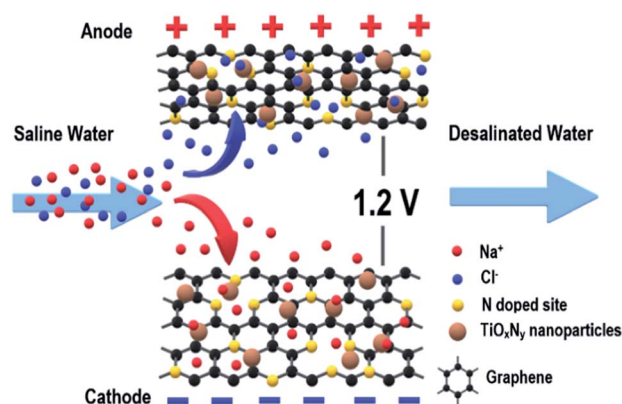

Fig. 1   Schematic of a flow-by CDI cell using $NG–TiO_xN_y$ electrodes.

potential range of −0.5 V to 0.5 V, representing both the cathode and anode adsorption processes. The experiment was conducted using an EC-lab SP-300 working station under the sweep rate range of 5–50 mV s^{-1} in 0.1–1 mol L^{-1} NaCl solution. The value of specific capacity of the prepared materials was calculated by integrating the area of the CV curve, using eqn (2):

$$C_s = \frac{\int I \mathrm{d}V}{2v\Delta Vm} \quad (2)$$

where C_s is the specific capacitance (F g^{-1}), I is the current (A), v is the scan rate (mV s^{-1}), Δv is the applied potential window (mV), and m is the electrode material mass (g). Electrochemical impedance spectroscopy (EIS) measurements were carried out at frequencies ranging from 100 kHz to 1 Hz. The amplitude of the alternating voltage was 10 mV, and the direct current potential was 0 V *vs.* open circuit potential.

2.4 CDI test

The synthesized NG–TiO$_x$N$_y$ electrode material with different mass ratios was mixed with PTFE and conductivity carbon (Super P) with a mass ratio of 8 : 1 : 1. The electrode material was dried in a vacuum oven and pressed on metal mesh with copper current collectors. Each plate had an effective surface area of 4 cm^2 and was separated by glass fiber with 5 mm space. Saline water with the salinity of 100–500 mg L^{-1} was fed into the cell by a peristaltic pump (Baoding Lange) and passed between two electrodes under the flowrate from 10–30 mL min^{-1}, and the potential from 0.8–1.2 V applied on each side. The salinity of the outflow water was measured by a CON6+ conductivity meter, and the raw data was converted into salinity using the calibration curve in Fig. S2.† The salt removal efficiency is calculated using the following eqn (3):

$$\eta = \frac{C_e}{C_{out}} \times 100\% \quad (3)$$

The salt adsorption capacity (SAC) was obtained using eqn (4):

$$SAC = \frac{(C_0 - C_e) \times V}{m} \quad (4)$$

where the C_0 is the initial concentration of the saline water, and C_e is the real-time concentration of the desalinated water. The maximum salt adsorption capacity is defined as the C_e at the lowest salt removal efficiency. m is the total mass of both electrodes and V is the real-time total saline water volume.

The salt adsorption rate (SAR) was calculated using eqn (5):

$$SAR = \frac{SAC}{t} \quad (5)$$

where t is the time corresponding to the SAC during the CDI desalination process.

3   Result and discussion

The XRD patterns of the synthesized NG–TiO$_x$N$_y$, rGO–TiO$_2$, and rGO are shown in Fig. 2a. For both NG–TiO$_x$N$_y$ and rGO–
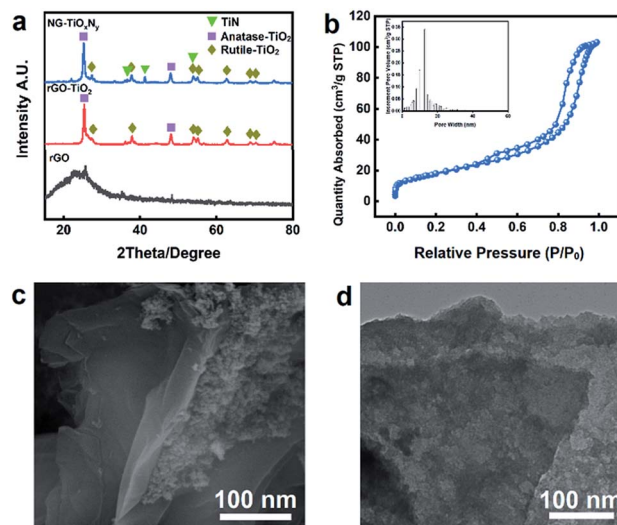

Fig. 2   (a) XRD patterns of NG–TiO$_x$N$_y$, rGO–TiO$_2$ and rGO; (b) N$_2$ adsorption–desorption isotherm and associated pore size distribution of NG–TiO$_x$N$_y$; (c) SEM image and (d) TEM image of NG–TiO$_x$N$_y$.

TiO$_2$, the main (101) peak at 25° and minor (200), (215) peaks at 48° and 75° can be assigned to the anatase-phase TiO$_2$ (JCPDS no. 21-1272), respectively. The peaks at 31°, 54°, 56°, can be assigned crystal planes (121), (211), (123) to the rutile-phase TiO$_2$ (JCPDS no. 46-1238). Both the presence of anatase-TiO$_2$ and rutile-TiO$_2$ are confirmed in the rGO–TiO$_2$ synthesized *via* hydrothermal method. New peaks appeared at 36°, 42°, and 62° indicated the successful nitridation of rGO–TiO$_2$ after ammonia annealing. The upshift of the characteristic peaks in the XRD pattern of NG–TiO$_x$N$_y$ as opposed to peaks for crystal planes (111), (200), (220) in standard TiN XRD profile (JCPDS: 38-1420, Fig. S3†) indicated the presence of the oxynitride. The value of N/Ti ratio (y) was calculated to be 0.61 (Table S1†), further proving the low degree of nitridation.[40–42] The XRD results prove the presence of various Ti species, including both the anatase-phase and rutile TiO$_2$ and the existence of TiO$_x$N$_y$ crystal phase. Based on previous reports, both anatase and rutile phase TiO$_2$ can have a positive effect on increasing the ion adsorption by increasing the wettability and forming a more cohesive EDL.[38,43] The calculated average size of the TiO$_x$N$_y$ nanoparticles was 43 nm. Such small size of nanoparticles can potentially provided more active sites for ion absorbing and forming the EDL on the surface of the nanoparticles.[43,44]

The BET analysis (Fig. 2b) shows a typical type IV isotherm curve, further confirmed the existence of the mesoporous

Table 1   BET surface area and pore volume of NG–TiO$_x$N$_y$ and rGO–TiO$_2$

	BET surface area (m^2 g^{-1})	BET pore volume (cm^3 g^{-1})
NG–TiO$_x$N$_y$	64.22	0.391
rGO–TiO$_2$	24.17	0.049

structure with the pore distribution around 18 nm. Compare with the rGO–TiO$_2$ (Table 1). The nitrogen doping process dramatically increased the BET surface area and the pore volume. The increase of the BET surface area is attributed to the loaded TiO$_x$N$_y$ nanoparticles with small crystal size and could be further explained by the surface vacancies generated during the ammonia heat treatment, which may result in a positive effect on ion absorbing.[45,46]

The SEM images in Fig. S4† at 1 μm magnitude indicates the layered structure of the graphene nanosheet. The layered nanosheets provide a relatively large surface area for interaction between liquid and solid as well as enough space for the saline water to pass through and assisted the ion diffusion process. Fig. 2c shows the TiO$_x$N$_y$ nanoparticles attached to the graphene nanosheet layer. The TiO$_x$N$_y$ nanoparticles provides the space for the formation of cohesive electrical double layer for ion absorbing. Fig. 2d is the TEM image of the synthesized NG–TiO$_x$N$_y$, which indicates the layered nanosheets of the graphene. Furthermore, the TiO$_x$N$_y$ nanoparticles embedded on graphene the layer further allows the absorption of saline water into the electrode structure, which extended the electrode–electrolyte interface into NG–TiO$_x$N$_y$ and minimized the distance of ion diffusion between the electrode surface and the saline water during the electrosorption process.

The elemental mapping (Fig. 3) suggests the homogenous distribution of the elements of the NG–TiO$_x$N$_y$ at 5 μm magnitude. The EDX mapping spectra reveals the mass ratio generally follows the rGO : TiO$_2$ = 2 : 1 as initial. Nitrogen accounts for 13.40% atomic percentage (Fig. 3b), demonstrating the nitrogen-enriched doped surface, which furthers the surface absorbing capacity.[46,47] To further study the chemical composition of the NG–TiO$_x$N$_y$ electrode material. X-ray photoelectron spectroscopy (XPS) was utilized, as shown in Fig. 4. The wide survey of the NG–TiO$_x$N$_y$, as shown in Fig. S5,† exhibits several main peaks assigned as Ti 2s, O 1s, Ti 2p, N 1s, C 1s, Ti 3s, and Ti 3p, respectively. The high resolution XPS spectrum of O 1s in Fig. 4a can be deconvoluted to Ti–O, C–O, –OH and O–C=O peaks, respectively. The formation of hydrogen bonds with water further enhanced the wettability of the electrode and had a positive effect on the ion storage process in the electrode material.[48,49] The XPS spectrum of C 1s scan in Fig. 4b is deconvoluted to the peaks of sp^2 C=C at 284.8 eV, sp^3 C–C peak at 286.8 eV, they are assigned to the C=C/C–C bond on the graphene aromatic ring. The peak at 287.4 eV and 289.2 eV are assigned to C=N and C–N bonds. Both demonstrate the successful nitrogen doping on the aromatic rings of graphene layer. The nitrogen configuration of the graphite layer can possibly result in a stronger binding energy with the ions in the electrolyte and enhancing the surface ion retention capacity.[50] Additionally, it is also reported the NG contributed to better wettability of the electrode material.[51] Thus, the presence of nitrogen doping graphene can be possible contributing to a higher salt adsorption capacity.[52] The carbon–oxygen peak at 291.3 eV is significantly diminished compared with the reported GO C 1s spectra,[53] which can be attributed to the reduction of oxygen on the GO nanosheets during the hydrothermal treatment. The nitrogen-doped graphite potentially contributes extra salt adsorption capacity during the CDI process by creating the surface vacancies.[54] The XPS spectrum of N 1s scan is presented in Fig. 4c, where the main peak at 396.3 eV and the peak at 397.4 eV assigned to Ti–N and Ti–O–N confirm the successful nitridation process of the Ti species. Such formation of the Ti–N and Ti–O–N bonds resulted in various Ti species, providing possibility for cation intercalation within the chemistry bonds and increased its adsorption capacity.[33,55] The peaks at 398.6 eV and 400.8 eV further confirm
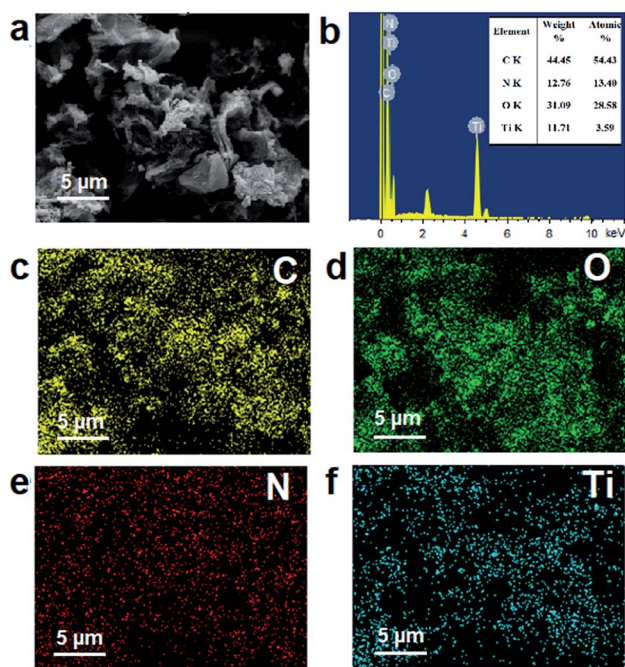

Fig. 3 (a) SEM images of NG–TiO$_x$N$_y$; (b) EDX spectrum of the NG–TiO$_x$N$_y$ associated with (a); elemental mapping of (c) C; (d) O; (e) N and (f) Ti.
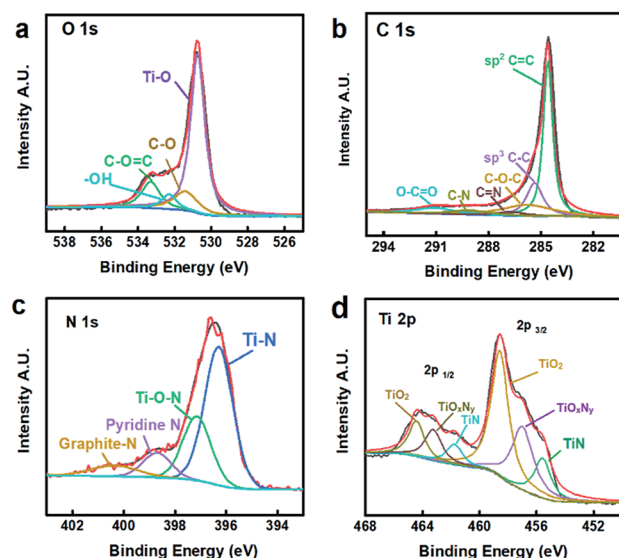

Fig. 4 High resolution XPS spectra of NG–TiO$_x$N$_y$ (a) C 1s scan; (b) O 1s scan; (c) N 1s scan; (d) Ti 2p scan.

the pyridine and graphite nitrogen doping sites. Fig. 4d illustrates the XPS spectrum of Ti 2p scan. The peaks at 458.8 eV and 456.8 eV are assigned to the Ti–O and the N intercalation into TiO_2 lattice or the formation of TiO_xN_y, respectively.[56] Both the N 1s scan and the Ti 2p scan confirmed the existing of oxygen and nitrogen species and the formation of oxynitride group in the TiO_xN_y, which is corresponded with the results in XRD analysis. The various Ti states of Ti potentially facilitate fast oxidation/reduction surface faradaic reactions during the electrochemical charge and discharge process, which provide an opportunity to effectively improve the specific capacitance and ion adsorption capacity.[57] Through the analysis of atomic percentages of different Ti species from the Ti 2p scan (Fig. S6†), the value of O/Ti ratio (x) is calculated as 0.66 (Table S2†). Thus, the composition of titanium compounds in this NG–TiO_xN_y nanocomposite (rGO : TiO_xN_y = 2 : 1 (w/w)) can be estimated as $TiO_{0.66}N_{0.61}$.

The CV curves were obtained at a wide range of scan rates (Fig. 5a) and in NaCl electrolyte solution with 3 different concentrations (Fig. 5c). All the CV curves of NG–TiO_xN_y are symmetric with respect to the x-axis and no significant oxidation/redox peaks were observed, indicating the reversibility of the EDL formation process dominated the electrosorption processes on the surface of the fabricated electrodes.[58] As calibrated in Fig. S1,† the symmetric CV curve shape of the CDI electrode is ranged from −0.5 V to 0.5 V

in actual, which indicates the electrode has the adsorption capacity for both Na^+ and Cl^-. To evaluate the electrochemical performance, the specific capacitance was calculated from the I–V plots, as shown in Fig. 5b. The specific capacitance ranges from 84.3–66.5 F g^{-1} as the scan rate increased from 10 to 50 mV s^{-1}. The decrease in the specific capacitance is possibly due to the charge-resistive behavior when the scan rate increased.[59] The mass ratio of N-doped graphene : TiO_xN_y is approximately 2 : 1, which results in a significant decrease of specific area and electrochemical active area as opposed to sole N-doped graphene and a further decrease of specific capacitance.[46,60,61] Fig. 5c shows the I–V curves for electrolyte solutions with concentrations of 0.1 mol L^{-1}, 0.5 mol L^{-1}, and 1 mol L^{-1}. Higher concentration of the electrolyte solution increased the mobility of the ions, while facilitated the formation of EDL on the electrode surface more easily.[62] Thus, the specific capacitance, ranging from 66.5–28.5 F g^{-1}, increased as the electrolyte concentration increased. In Fig. 5d after 5000 CV cycles with at the scan rate of 50 mV s^{-1}, the NG–TiO_xN_y electrode retained 90% to its initial capacitance, demonstrating its excellent electrochemical stability. Fig. 5e presents the comparison of NG–TiO_xN_y with commercial AC electrode, pure rGO, and rGO–TiO_2 (initial mass ratio 2 : 1). As can be seen from the figure, NG–TiO_xN_y showes higher specific capacitance at the scan rate of 50 mV s^{-1} than the AC, rGO and rGO–TiO_2 electrodes. The higher capacitance can be attributed to the nitrogen-doped sites on the graphene layer and the surface vacancies generated during the Ti species nitridation.[46,63] Electrochemical Impedance Spectroscopy (EIS) analysis, which is usually used for evaluating the electrical conductivity of electrode materials, was performed to further investigate the electrochemical properties of the synthesized NG–TiO_xN_y. The Nyquist plots for the electrode material are shown in Fig. 5f, where the typical semicircles can be observed, representing low resistance of the electrode/electrolyte interface and its high capacitance. The slope after the semicircle indicates the formation of the electrical double layer on the surface of the electrode material.[49] Compared with AC, rGO, and rGO–TiO_2 electrodes, the higher slope and smaller semicircle of NG–TiO_xN_y indicates its higher diffusion coefficient and smaller diffusion resistance for the adsorbed ions.[64] Such phenomena can be explained by the formation of the surface oxygen vacancies and the capacitance from oxygen vacancies ion adsorption during ammonia heat treatment.[65]

The whole CDI process can be seen in Fig. S6.† The mass ratio graphite and Ti species were optimized by preliminary desalination experiments using different rGO : TiO_2 mass ratios as shown in Fig. 6a. Compared to the pristine rGO, rGO–TiO_2, and AC, the NG–TiO_xN_y material exhibited significantly lower salt retention rate, which is less than 50% at 25 min. The higher performance of NG–TiO_xN_y can be attributed to the enhanced ion absorbing capacity due to the nitrogen doping process with higher binding capacity between nitrogen doping sites and the ions,[33,46] which is also corresponded with the better electrochemical performance. Furthermore, the higher CDI performance of the electrodes after nitrogen doping can be explained enhanced ions storage capacity in the surface vacancies formed during the ammonia heat treatment.[54] The optimized initial mass ratio of rGO : TiO_2 = 2 : 1 was chosen for further study. Compared with rGO–TiO_2 (initial mass ratio 2 : 1), the n-doping
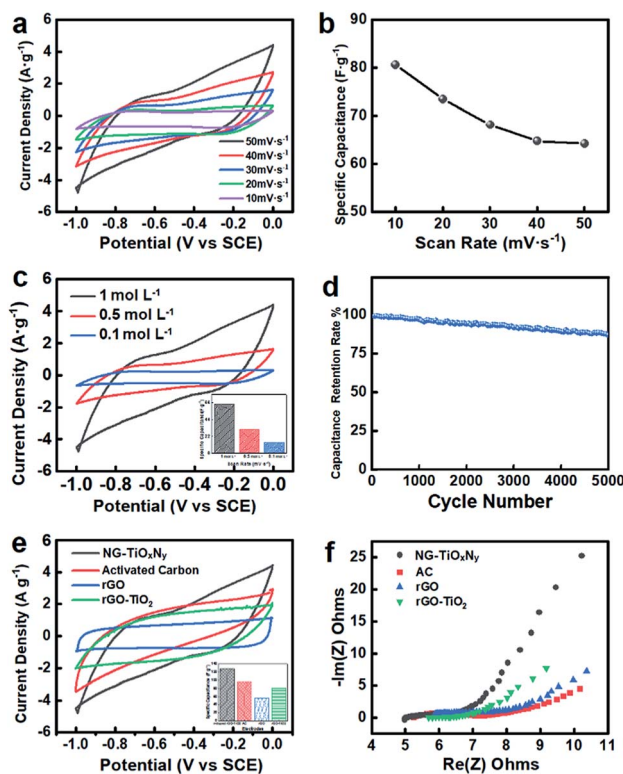

Fig. 5 (a) CV curves of NG–TiO_xN_y electrode with scan rates of 10, 20, 30, 40, and 50 mV s^{-1}; (b) specific capacitance of NG–TiO_xN_y vs. scan rate. (c) CV curves of NG–TiO_xN_y with 0.1 mol L^{-1}, 0.5 mol L^{-1}, and 1 mol L^{-1} aqueous NaCl solutions; (d) cycling stability test for 5000 cycles; (e) CV curves and specific capacitance of NG–TiO_xN_y, AC, rGO and rGO–TiO_2; (f) EIS Nyquist plots of NG–TiO_xN_y, AC, rGO and rGO–TiO_2.
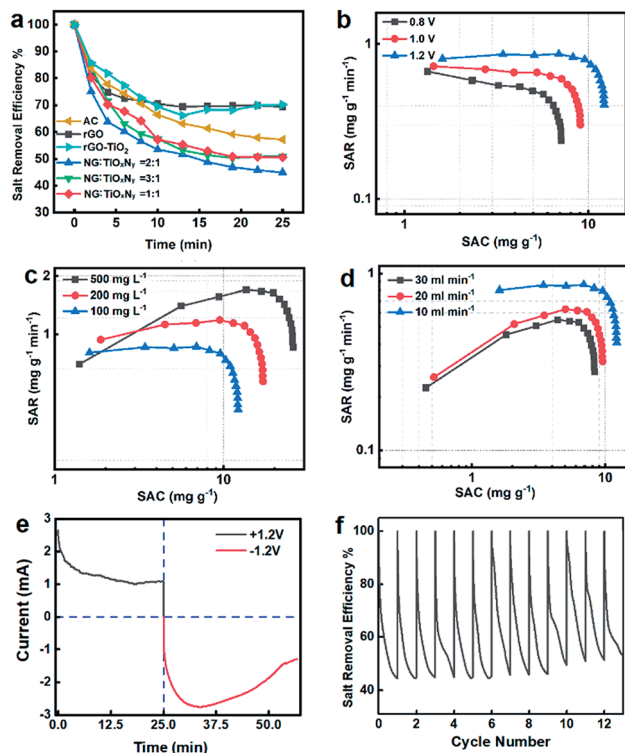
Fig. 6 (a) Comparison of salt retention curves of electrodes NG : TiOxNy = 1 : 1 to 3 : 1, rGO, and AC; Ragone plots of NG−TiOxNy at: (b) potential of 0.8 V, 1.0 V and 1.2 V; (c) water salinity of 500 mg L^{-1}, 200 mg L^{-1}, and 100 mg L^{-1}; (d) flow rates of 30 mL min^{-1}, 20 mL min^{-1} and 10 mL min^{-1}; (e) current vs. time plot; (f) cycling stability for over 12 cycles.

and nitridation process significantly enhanced the salt adsorption capacity of the NG–TiOxNy CDI electrode material. The dramatically high salt efficiency of NG–TiOxNy can be attributed the multi-layered graphene nanosheets facilitated the rapid liquid diffusion; higher specific capacitance and the surface adsorption and ion intercalation within the Ti–O–N lattice.[57,66]

Fig. 6b–d shows the Ragone plots of SAC vs. SAR under different working conditions.[67] In all the three tests, the SAC increases rapidly during the first 5 min and gradually reached

saturated after 25 min, while the SAR follows the same pattern. Fig. 6b shows the batch-mode CDI test was performed at 10 mL min^{-1} flow rate with 100 mg L^{-1} NaCl solution. The SACs reaches equilibrium approximately 8.1 mg g^{-1}, 9.6 mg g^{-1}, and 12.8 mg g^{-1} with cell voltages of 1.2-0.8 V at near saturated adsorption, respectively. Meanwhile, the SAR of each group at initial stage reached 0.7–0.95 mg g^{-1} min^{-1}. The increase in the SACs and SARs indicated that the salt adsorption capacity was strongly depended on potential applied on the cell, which will result in a more cohesive electrical double layer and enhance the ion absorbing capacity.[68] In Fig. 6c, the SACs were obtained with 10 mL min^{-1} flow rate and 1.2 V while the salinity of the pumped-in water concentrations ranges from 100–500 mg L^{-1}. Despite the increase in saline water concentration, the electrode maintained its salt adsorption capacity, demonstrating the possibility of its application in high salt concentrations treatment. At the salt concentration of 500 mg L^{-1}, the salt adsorption capacity reached a breakthrough SAC of 26.1 mg g^{-1} at its near saturation adsorption. It is also worth to mention the SAR of 500 mg L^{-1} saline water group reached as high as 1.8 mg g^{-1} min^{-1}, which is considerable high SAR compared with previous reports.[67] Fig. 6d shows the SACs for different flow rates (10–30 mL min^{-1}) at 1.2 V and salt concentration of 100 mg L^{-1}. The SAC curves have a similar trend as the previous experiments, and the SACs were 12.6–7.0 mg g^{-1} while the SARs were 0.95–0.45 mg g^{-1} min^{-1} at near saturated adsorption, respectively. The relatively smaller SAC declines when performing the CDI test in higher flowrates enabled its potential in fast water desalination. Fig. 6e shows the current-elapsed time curve, which directly corresponded to the conductivity and salt removal efficiency curve by measuring the current at the outflow stream. The potential applied to the CDI cell shifted from 1.0 V to −1.0 V at 25 minutes. The current curve quickly dropped in the first 10 minutes, and then reached the lowest current at 25 minutes. The conductivity of the outflow water recovered slightly and reached the saturation point of ions adsorption. The potential was shifted at 25 minutes, resulting in a rapid increase in reverse current, showing the release of ions from the porous electrode. The negative current then decreased after a few minutes, which indicated that the reverse adsorption

Table 2 SAC comparison of commercial AC, typical carbon electrodes, n-doped carbon and titanium-based CDI electrodes

Electrode	Cell voltage V	Salinity mg L^{-1}	SAC mg g^{-1}	Ref
Commercial AC	1.2	292–1170	10.9–13.0	70
Carbon aerogel	1.2	100–1000	5–15	71
Graphene and derivatives	0.8–1.2	100–1000	5–20	72
rGO–TiO$_2$	1.2	300	9.2–13.2	73
CNT–TiO$_2$	1.2	500	~4.3	74
TiO$_2$–AC	1.2	500	~2.7	75
TiO$_2$ NPs/AC	1.2	100	~8.04	69
Ti$_3$C$_2$–mxene	1.2	100	13	76
Ti$_3$C$_2$T$_x$–mxene	1.2	500	20–24	77
N-doped graphene	1.2	500	>17.8	78
N-doped carbon sphere	1.2	1000	14.91	79
N-doped TiO$_2$/ZrO$_2$	1.2	50	3.98	80
3DOM–TiN	1.2	500	25.3	34
NG–TiOxNy	1.2	500	26.1	This work

process occurred. The rapid charge and discharge performance of the NG–TiO$_x$N$_y$ electrode demonstrated its great potential in ad/desorption potential. In Fig. 6f, the regeneration test was performed using NaCl saline water with 10 mL min^{-1} flow rate and 100 mg L^{-1} salt concentration and repeated charge–discharge cycles for 30 minutes. The salt removal efficiency remained at 90% of its original capacity for over 12 cycles which is superior than most reported titanium-based CDI electrodes.[43,69] The stable cycling stability demonstrated that the synthesized NG–TiO$_x$N$_y$ has an excellent potential for longtime-continuous desalination application. Compared with several reported porous carbon and titanium-carbon electrode materials (Table 2), the NG–TiO$_x$N$_y$ material in this work exhibites significantly higher salt adsorption capacity.

4 Conclusions

In this work, we successfully synthesized a novel type of nitrogen-doped graphene–titanium oxynitride (NG–TiO$_x$N$_y$) nanocomposite electrode *via* hydrothermal reaction and high-temperature nitridation process and then tested for CDI. The physical and chemicalcharacterization revealed the nitrogen was successfully doped onto the graphite layer and formed various species of nitrogen-doped carbon. Additionally, the TiO$_x$N$_y$ nanoparticles were also formed and embedded on the graphene nanosheets. Further study revealed the ammonia treatment and the loaded TiO$_x$N$_y$ nanoparticles gave the electrode better electrochemical performance and extra ion absorbing capacity compared with graphene and TiO$_2$ based CDI electrodes. Consequently, the multi-layered graphene nanosheets allowed the saline water stream to pass through the electrodes and absorbing ions in both the surface of nitrogen-doped graphene and TiO$_x$N$_y$ nanoparticles. In the batch mode CDI test, the NG–TiO$_x$N$_y$ electrode-based CDI device exhibited a significantly high salt adsorption capacity of 26.1 mg g^{-1} at its near saturated adsorption using 500 mg L^{-1} feed-in saline water. In the cycling stability test, the NG–TiO$_x$N$_y$ electrode lasted for over 12 cycles while retaining over 90% of its original salt removal capacity, furthers its great potential in long-time continuous CDI application.

Conflicts of interest

There are no conflicts to declare.

Acknowledgements

References

1 M. Catley-Carlson, *Nature*, 2011, **473**, 27.

2 F. A. AlMarzooqi, A. A. Al Ghaferi, I. Saadat and N. Hilal, *Desalination*, 2014, **342**, 3–15.

3 Y. H. Teow and A. W. Mohammad, *Desalination*, 2019, **451**, 2–17.

4 S. Santangelo, *Appl. Sci.*, 2019, **9**, 1049.

5 Y. Oren, *Desalination*, 2008, **228**, 10–29.

6 J. Oladunni, J. H. Zain, A. Hai, F. Banat, G. Bharath and E. Alhseinat, *Sep. Purif. Technol.*, 2018, **207**, 291–320.

7 S. Porada, R. Zhao, A. van der Wal, V. Presser and P. M. Biesheuvel, *Prog. Mater. Sci.*, 2013, **58**, 1388–1442.

8 K. Shi and I. Zhitomirsky, *ChemElectroChem*, 2015, **2**, 396–403.

9 K. Tang, J. Chang, H. Cao, C. Su, Y. Li, Z. Zhang and Y. Zhang, *ACS Sustainable Chem. Eng.*, 2017, **5**, 11324–11333.

10 F. Duan, X. Du, Y. Li, H. Cao and Y. Zhang, *Desalination*, 2015, **376**, 17–24.

11 K. Shi, X. Yang, E. D. Cranston and I. Zhitomirsky, *Adv. Funct. Mater.*, 2016, **26**, 6437–6445.

12 G. Divyapriya, K. K. Vijayakumar and I. Nambi, *Desalination*, 2019, **451**, 102–110.

13 Z. U. Khan, T. Yan, L. Shi and D. Zhang, *Environ. Sci.: Nano*, 2018, **5**, 980–991.

14 J. Han, L. Shi, T. Yan, J. Zhang and D. Zhang, *Environ. Sci.: Nano*, 2018, **5**, 2337–2345.

15 H.-J. Choi, S.-M. Jung, J.-M. Seo, D. W. Chang, L. Dai and J.-B. Baek, *Nano Energy*, 2012, **1**, 534–551.

16 J. H. Chang, A. Huzayyin, K. Lian and F. Dawson, *Appl. Phys. Lett.*, 2015, **107**, 193902.

17 Z. Luan, Y. Tian, L. Gai, H. Jiang, X. Guo and Y. Yang, *J. Alloys Compd.*, 2017, **729**, 9–18.

18 Y. He, W. Chen, X. Li, Z. Zhang, J. Fu, C. Zhao and E. Xie, *ACS Nano*, 2013, **7**, 174–182.

19 A. Abdelkader and D. Fray, *Nanoscale*, 2017, **9**, 14548–14557.

20 W. Dianbudiyanto and S.-H. Liu, *Desalination*, 2019, **468**, 114069.

21 H. Tian, N. Wang, F. Xu, P. Zhang, D. Hou, Y. Mai and X. Feng, *J. Mater. Chem. A*, 2018, **6**, 10354–10360.

22 H. Gao, J. Li and K. Lian, *RSC Adv.*, 2014, **4**, 21332–21339.

23 X. Xu, Z. Sun, D. H. Chua and L. Pan, *Sci. Rep.*, 2015, **5**, 11225.

24 W. Niu and Y. Yang, *ACS Energy Lett.*, 2018, **3**, 2796–2815.

25 W. Niu and Y. Yang, *ACS Appl. Energy Mater.*, 2018, **1**, 2440–2445.

26 W. Lei, J. Guo, Z. Wu, C. Xuan, W. Xiao and D. Wang, *Science Bulletin*, 2017, **62**, 1011–1017.

27 W. Lei, L. Han, C. Xuan, R. Lin, H. Liu, H. L. Xin and D. Wang, *Electrochim. Acta*, 2016, **210**, 130–137.

28 X. Cao, G. Tian, Y. Chen, J. Zhou, W. Zhou, C. Tian and H. Fu, *J. Mater. Chem. A*, 2014, **2**, 4366–4374.

29 J. Kim, W.-H. Khoh, B.-H. Wee and J.-D. Hong, *RSC Adv.*, 2015, **5**, 9904–9911.

30 Y.-J. B. Ting, K. Lian and N. Kherani, *ECS Trans.*, 2011, **35**, 133–139.

31 G. Lui, G. Li, X. Wang, G. Jiang, E. Lin, M. Fowler, A. Yu and Z. Chen, *Nano Energy*, 2016, **24**, 72–77.

32 L. Chen, H. Dai, Y. Zhou, Y. Hu, T. Yu, J. Liu and Z. Zou, *Chem. Commun.*, 2014, **50**, 14321–14324.

33 A. Achour, M. Chaker, H. Achour, A. Arman, M. Islam, M. Mardani, M. Boujtita, L. Le Brizoual, M. Djouadi and T. Brousse, *J. Power Sources*, 2017, **359**, 349–354.

34 Y. Wu, G. Jiang, G. Liu, G. Lui, Z. Cano, Q. Li, Z. Zhang, A. Yu, J. Zhang and Z. Chen, *J. Mater. Chem. A*, 2019, **7**, 15633–15639.

35 Z. Liu, Z. Jin, X. Liu, Y. Fu and G. Liu, *J. Sol-Gel Sci. Technol.*, 2006, **38**, 73–78.

36 S. Sung, S. Park, W.-J. Lee, J. Son, C.-H. Kim, Y. Kim, D. Y. Noh and M.-H. Yoon, *ACS Appl. Mater. Interfaces*, 2015, **7**, 7456–7461.

37 O. Wiranwetchayan, S. Promnopas, T. Thongtem, A. Chaipanich and S. Thongtem, *Surf. Coat. Technol.*, 2017, **326**, 310–315.

38 C. Kim, J. Lee, S. Kim and J. Yoon, *Desalination*, 2014, **342**, 70–74.

39 S. Pei and H.-M. Cheng, *Carbon*, 2012, **50**, 3210–3228.

40 I. G. Morozov, O. Belousova, O. Belyakov, I. Parkin, S. Sathasivam and M. Kuznetcov, *J. Alloys Compd.*, 2016, **675**, 266–276.

41 R. A. Sait and R. B. M. Cross, *Appl. Surf. Sci.*, 2017, **424**, 290–298.

42 C.-L. Lee, C. Kim and I.-D. Kim, *RSC Adv.*, 2017, **7**, 44804–44808.

43 M. Ding, S. Fan, S. Huang, M. E. Pam, L. Guo, Y. Shi and H. Y. Yang, *ACS Appl. Energy Mater.*, 2019, **2**, 1812–1822.

44 D. Guo, R. Shibuya, C. Akiba, S. Saji, T. Kondo and J. Nakamura, *Science*, 2016, **351**, 361–365.

45 G. Liu, J. Li, J. Fu, G. Jiang, G. Lui, D. Luo, Y. P. Deng, J. Zhang, Z. P. Cano and A. Yu, *Adv. Mater.*, 2018, 1806761.

46 P. Bharathidasan, S. Sridhar, P. V. Vardhan, S. Sivakkumar, D.-W. Kim and S. Devaraj, *J. Mater. Sci.: Mater. Electron.*, 2018, **29**, 7661–7667.

47 Y. Liu, T. Chen, T. Lu, Z. Sun, D. H. C. Chua and L. Pan, *Electrochim. Acta*, 2015, **158**, 403–409.

48 M. Hashemi, M. S. Rahmanifar, M. F. El-Kady, A. Noori, M. F. Mousavi and R. B. Kaner, *Nano energy*, 2018, **44**, 489–498.

49 A. S. Yasin, H. O. Mohamed, I. M. Mohamed, H. M. Mousa and N. A. Barakat, *Sep. Purif. Technol.*, 2016, **171**, 34–43.

50 L.-F. Chen, X.-D. Zhang, H.-W. Liang, M. Kong, Q.-F. Guan, P. Chen, Z.-Y. Wu and S.-H. Yu, *ACS Nano*, 2012, **6**, 7092–7102.

51 W. Xiong, M. Liu, L. Gan, Y. Lv, Z. Xu, Z. Hao and L. Chen, *Colloids Surf., A*, 2012, **411**, 34–39.

52 K. Wang, L. Li, T. Zhang and Z. Liu, *Energy*, 2014, **70**, 612–617.

53 B. Yu, X. Wang, X. Qian, W. Xing, H. Yang, L. Ma, Y. Lin, S. Jiang, L. Song and Y. Hu, *RSC Adv.*, 2014, **4**, 31782–31794.

54 W. Lei, W. Xiao, J. Li, G. Li, Z. Wu, C. Xuan, D. Luo, Y.-P. Deng, D. Wang and Z. Chen, *ACS Appl. Mater. Interfaces*, 2017, **9**, 28604–28611.

55 Z. Lei, N. Christov and X. Zhao, *Energy Environ. Sci.*, 2011, **4**, 1866–1873.

56 M. S. Akple, J. Low, Z. Qin, S. Wageh, A. A. Al-Ghamdi, J. Yu and S. Liu, *Chin. J. Catal.*, 2015, **36**, 2127–2134.

57 G. Hasegawa, A. Kitada, S. Kawasaki, K. Kanamori, K. Nakanishi, Y. Kobayashi, H. Kageyama and T. Abe, *J. Electrochem. Soc.*, 2015, **162**, A77–A85.

58 G. Trefalt, S. H. Behrens and M. Borkovec, *Langmuir*, 2015, **32**, 380–400.

59 S. Karade, D. Dubal and B. Sankapal, *MoS₂ ultrathin nanoflakes for high performance supercapacitors: Room temperature chemical bath deposition (CBD)*, 2016.

60 C. Xiang, M. Li, M. Zhi, A. Manivannan and N. Wu, *J. Mater. Chem.*, 2012, **22**, 19161–19167.

61 J. Lazarte, R. Dipasupil, G. Pasco, R. Eusebio, A. Orbecido, R.-a. Doong and L. Bautista-Patacsil, *Nanomaterials*, 2018, **8**, 934.

62 K.-C. Tsay, L. Zhang and J. Zhang, *Electrochim. Acta*, 2012, **60**, 428–436.

63 A. Achour, J. Ducros, R. Porto, M. Boujtita, E. Gautron, L. Le Brizoual, M. Djouadi and T. Brousse, *Nano Energy*, 2014, **7**, 104–113.

64 Z. Xing, G. Li, S. Sy and Z. Chen, *Nano Energy*, 2018, **54**, 1–9.

65 M. Inagaki, M. Toyoda, Y. Soneda and T. Morishita, *Carbon*, 2018, **132**, 104–140.

66 C. Zhu, P. Yang, D. Chao, X. Wang, X. Zhang, S. Chen, B. K. Tay, H. Huang, H. Zhang and W. Mai, *Adv. Mater.*, 2015, **27**, 4566–4571.

67 T. Kim and J. Yoon, *RSC Adv.*, 2015, **5**, 1456–1461.

68 J. Zhang, J. Fang, J. Han, T. Yan, L. Shi and D. Zhang, *J. Mater. Chem. A*, 2018, **6**, 15245–15252.

69 P.-I. Liu, L.-C. Chung, H. Shao, T.-M. Liang, R.-Y. Horng, C.-C. M. Ma and M.-C. Chang, *Electrochim. Acta*, 2013, **96**, 173–179.

70 R. Zhao, P. M. Biesheuvel, H. Miedema, H. Bruning and A. van der Wal, *J. Phys. Chem. Lett.*, 2010, **1**, 205–210.

71 A. Thamilselvan, A. Nesaraj and M. Noel, *Int. J. Environ. Sci. Technol.*, 2016, **13**, 2961–2976.

72 H. Yin, S. Zhao, J. Wan, H. Tang, L. Chang, L. He, H. Zhao, Y. Gao and Z. Tang, *Adv. Mat.*, 2013, **25**, 6270–6276.

73 A. G. El-Deen, J.-H. Choi, C. S. Kim, K. A. Khalil, A. A. Almajid and N. A. Barakat, *Desalination*, 2015, **361**, 53–64.

74 H. Li, Y. Ma and R. Niu, *Separation and Purification Technology*, 2016.

75 P. Srimuk, M. Zeiger, N. Jäckel, A. Tolosa, B. Krüner, S. Fleischmann, I. Grobelsek, M. Aslan, B. Shvartsev and M. E. Suss, *Electrochim. Acta*, 2017, **224**, 314–328.

76 P. Srimuk, F. Kaasik, B. Krüner, A. Tolosa, S. Fleischmann, N. Jäckel, M. C. Tekeli, M. Aslan, M. E. Suss and V. Presser, *J. Mater. Chem. A*, 2016, **4**, 18265–18271.

77 W. Bao, X. Tang, X. Guo, S. Choi, C. Wang, Y. Gogotsi and G. Wang, *Joule*, 2018, **2**, 778–787.

78 M. Mi, X. Liu, W. Kong, Y. Ge, W. Dang and J. Hu, *Desalination*, 2019, **464**, 18–24.

79 Y. Liu, T. Chen, T. Lu, Z. Sun, D. H. Chua and L. Pan, *Electrochim. Acta*, 2015, **158**, 403–409.

80 A. S. Yasin, I. M. Mohamed, H. M. Mousa, C. H. Park and C. S. Kim, *Sci. Rep.*, 2018, **8**, 541.